Technical Capabilities of the Large Millimeter Telescope *Alfonso Serrano*

F. Peter Schloerb

Department of Astronomy
University of Massachusetts Amherst

1. INTRODUCTION

This paper is intended to provide details about the current status of the Large Millimeter Telescope (LMT) in support of the recent submission of a white paper about the facility to the ASTRO 2020 Decadal Survey in the United States.

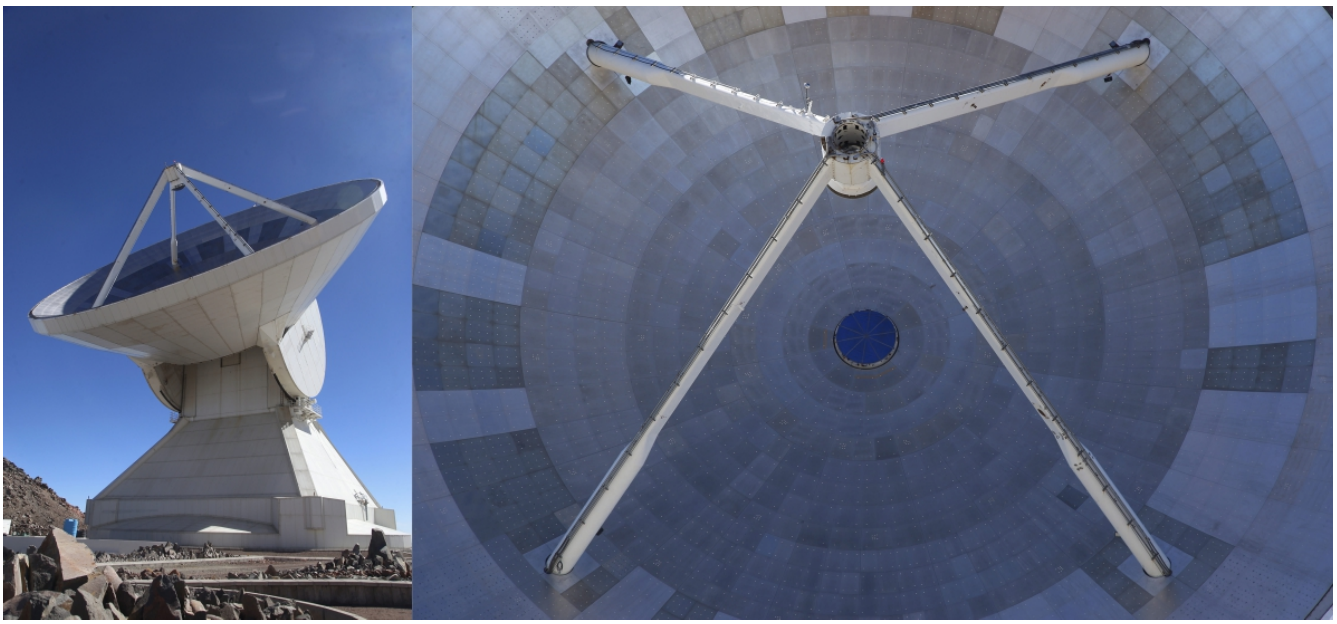

Figure 1 – (Left Panel) View of the 50m-diameter Large Millimeter Telescope. (Right Panel) View of the inner part of the antenna.

2. SUMMARY OF ANTENNA DEVELOPMENT HISTORY

The binational LMT project has had a long period of development. Construction of the antenna began at the LMT site in the year 2000, and the steel structure was completed in 2006. In 2008, the Mexican Government provided the necessary funding to bring the telescope into operation following the installation of the inner 32m of its primary surface. This effort culminated in 2011 with the detection of "first light" at millimeter wavelengths by the antenna. However, at that time it became apparent that the telescope was not performing to its original design specifications. Thus, under new management, a program to rehabilitate the 32m-diameter surface was initiated resulting in the achievement of excellent performance and the demonstration of the LMT's capabilities in a campaign of "Early Science".

The success of the Early Science results led the Mexican Government to approve an additional investment to complete the full 50m-diameter surface as well as upgrade other optical and electromechanical systems. One of the major upgrades required the design and installation of a new secondary mirror and hexapod. The full 50m-diameter primary reflector and its active surface control system was completed in early 2018. The LMT Collaboration is now completing the final alignment and commissioning of the antenna and its instrumentation and beginning initial science observations..

3. ANTENNA SURFACE

3.1 Description

The LMT primary reflector consists of 180 individual surface segments. The segments are arranged in 5 annular rings with 12, 24, 48, 48, and 48 segments in rings 1 to 5 respectively. Each segment has four actuators at the corners to allow the primary reflector to adapt to gravitational deformations, as the elevation is changed, and thermally induced distortions.

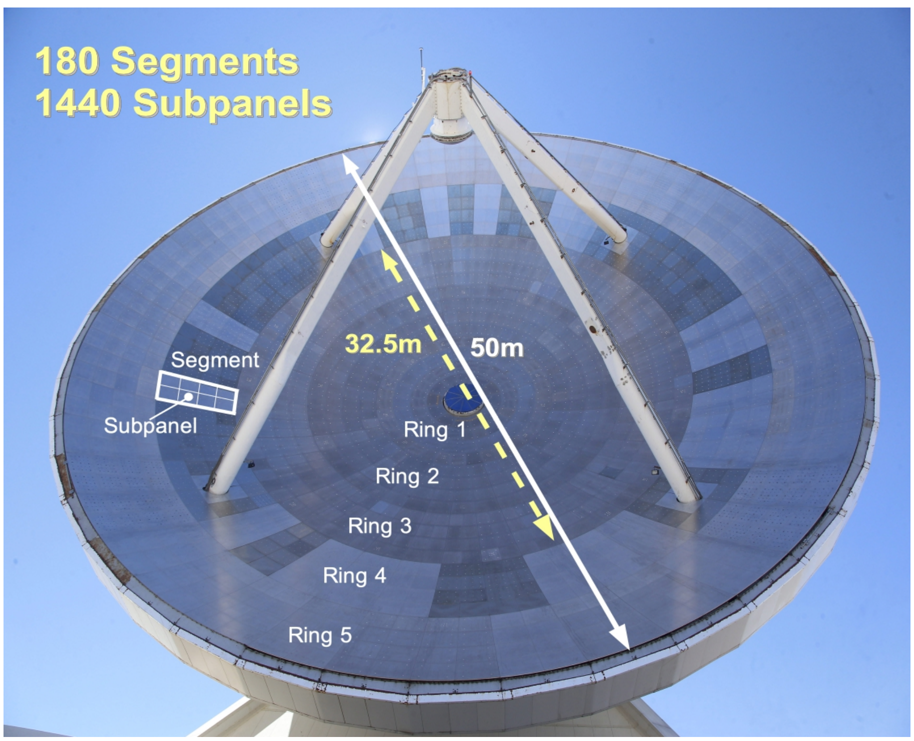

Figure 2. The complete 50m-diameter primary reflector with active control to correct gravitational and thermal deformations. The 180 segments are located in 5 concentric rings. The three inner rings cover 32-m in diameter. As part of the "GTM Completion Plan", we installed a new secondary mirror and ihexapod, and concluded the expansion of the active primary reflector from 32-m to 50-m in diameter in March 2018. Currently the primary reflector is in the process of optimizing its global alignment and implementation of the correction model to maximize its performance when moving in elevation.

Each of the LMT's segments is comprised of 8 high precision "subpanels," which are assembled and aligned in the laboratory using a laser tracker (Gale et al

2018a).   After “first light” with the telescope in 2011, it was determined that the internal alignment of the segments required substantial improvement for the LMT to reach its goals. Figure 3 shows the evolution of improvements in the alignment results achieved for reflector segments in the primary surface of the 50 m diameter GTM. A major engineering effort coordinated in 2012 and 2013 led to the reinstallation of segments in rings 1, 2, and 3 with accuracies of approximately 30 microns rms, as shown in Figure 3.   Not all segments were replaced at this time, and 17 of the 48 segments in ring 3 still need to be rehabilitated.

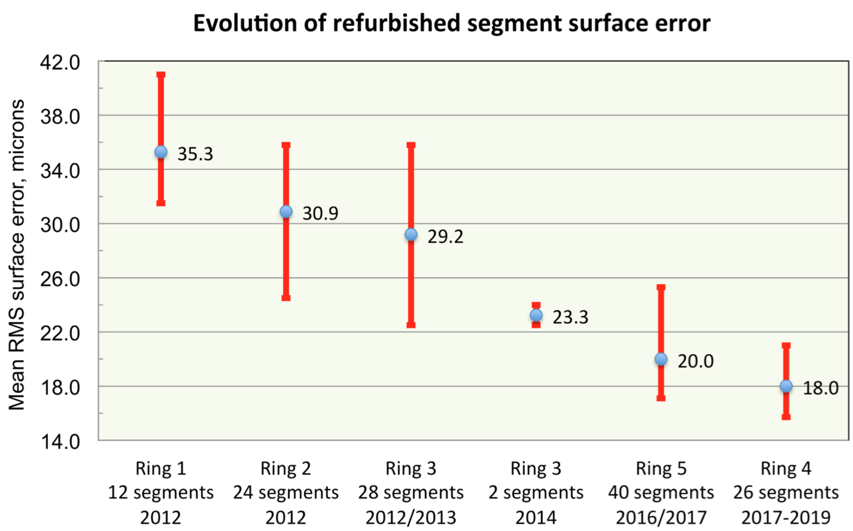

Figure 3. The evolution of the improvements in the alignment accuracy of the reflector segments on the primary surface of the 50m-diameter LMT.

Figure 3 also shows the most recent improvements in the alignment accuracy of segments integrated in 2016-2017 and installed in rings 4 and 5. This improvement is due to the selection of new materials and better quality control in the manufacturing of the individual adjusting components. Improvements in the laser tracker metrology system have also contributed to final alignments of individual segments with greater precision.   It should be noted that not all segments in ring 4 were completed using the new processes through 2019. At this time, there remain 14 segments in ring 4 that are to be upgraded to achieve the full precision that is possible.

Considering the successful demonstration of our enhanced ability to manufacture and align segments in rings 4 and 5, it will be possible, without any technical or engineering risk, to provide similar precision in the alignment accuracy in the inner three rings. This will increase the overall operation and performance of the telescope, particularly at the shortest wavelengths.

3.2 Surface Alignment

Once segments are installed on the antenna, they are aligned globally within the antenna backup structure using the technique of photogrammetry. A general description of the technique and results is provided in Gale et al (2018b). Individual targets are placed on the primary mirror, with approximately 32 targets on each individual segment. The three-dimensional point cloud of the positions of all targets, produced by the photogrammetry camera, is fit to a best parabola, and, for each segment, residuals to the fit are used to determine the optimum settings for the segment's actuators. Photogrammetry measurements are carried out at night to minimize changes in the surface due to thermal deformation.

Early photogrammetry work setting the inner 3 rings of the antenna yielded excellent results with an overall optical rms for the telescope of about 85 microns and allowed the project to demonstrate the use of the antenna's active surface. The left panel of Figure 4 shows the antenna gain at 1.1 millimeters wavelength with the AzTEC instrument as a function of elevation angle. Near-constant gain over the full elevation range of the telescope illustrates the effectiveness of the LMT's active surface.

The right panel of Figure 4 illustrates another feature of the use of the LMT's active surface that was demonstrated in initial work with the 32m-diameter surface. Surface setting measurements showed that the antenna deformed during the night due to thermal gradients within the telescope structure. The main thermal distortion is a vertical astigmatism on the dish, and so it became possible to solve for this effect with measurements of the beam pattern during the night. The individual beam pattern maps and peak gain illustrate how, with regular measurements, it is possible to track the thermal behavior (Schloerb et al 2016).

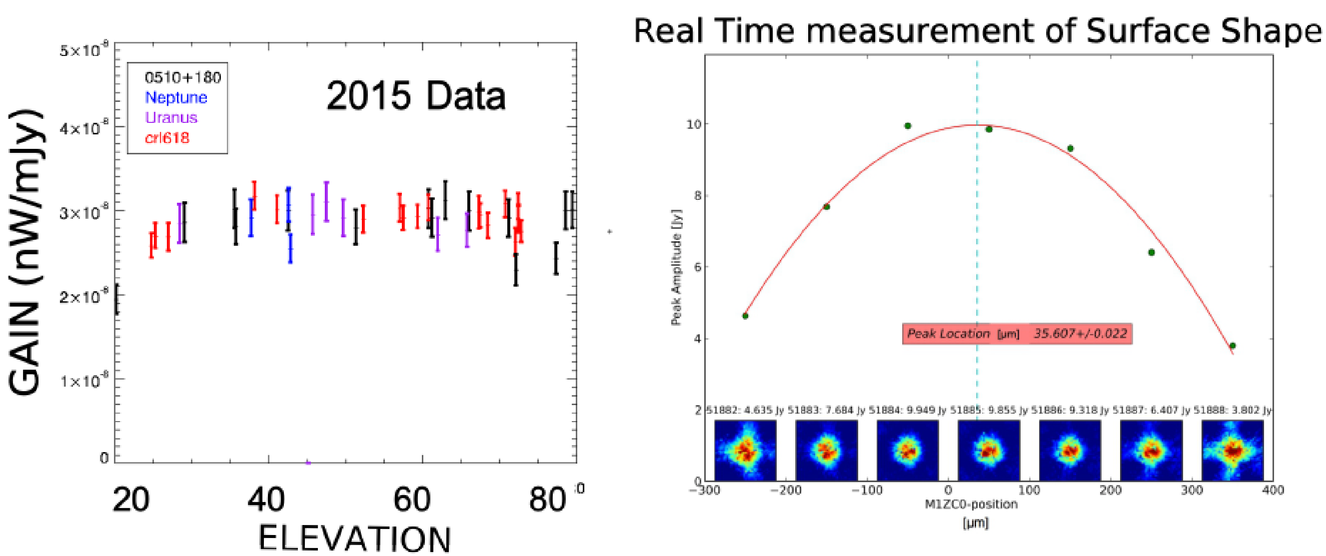

Figure 4 – Demonstration of the 32m-diameter LMT active surface. The left panel shows the antenna gain at 1.1 millimeters wavelength with the AzTEC instrument as a function of elevation angle. The right panel shows measurements made to optimize the antenna surface shape in order to counteract the effect of thermal deformations of the antenna. The shape of the antenna surface is intentionally deformed according to the Zernike polynomial for vertical astigmatism and the gain and beam pattern are measured to find the optimum value (Schloerb et al 2016).

Figure 5 shows an example of a single surface iteration of the full 50m-diameter surface obtained in February 2018 shortly after completion of the active surface installation. In this example, the photogrammetry data were processed to derive the best positions of the actuators at the corners of the segments and then these best positions were automatically fed back to the actuator control system to adjust the surface for a new measurement and iteration. The technique can quickly (within about 1 hour) measure the shape of the surface and derive new actuator positions.

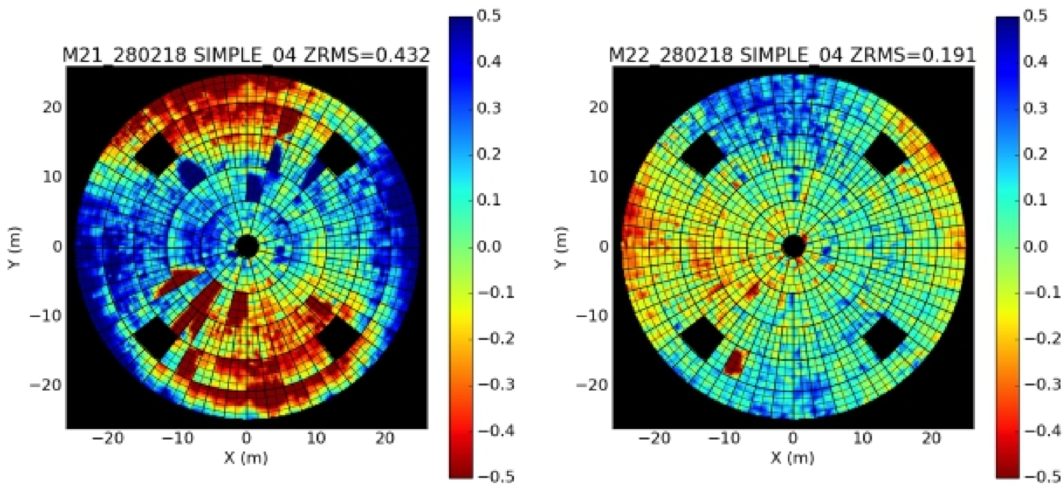

Figure 5 – Initial LMT surface measurements after completion of the full 50m surface, obtained on February 28, 2018. The left map shows the surface errors with respect to best fitting parabola before adjustments. The right map shows the improvement after one iteration.

3.3 Estimate of Photogrammetry Measurement Errors

We may establish an estimate of the measurement errors for the photogrammetry data by looking at the repeatability of two consecutive maps. Figure 6 shows the difference between two consecutive maps along with a histogram of the differences between positions of the targets. The target differences are 77 microns rms in the location of the target along the z-axis (optical axis) of the parabola, which would correspond to a measurement error for targets of about 55 microns rms.

We may also derive actuator positions from each map and take those differences as well. This result is shown in the right hand panel of Figure 6 and gives an rms of about 90 microns.   So, based on repeatability of the results of deriving actuator position over the full antenna, we may assign an error of about 64 microns rms for the determination of positions of individual actuators.

It should be noted, however, that the difference map itself (Figure 6: left hand panel) has regional highs and lows which are not consistent with random errors. Moreover, independent estimates of the photogrammetry measurement error suggest that errors should be on the order of 40 microns. This suggests that some of the difference that is observed might be due either to: (1) systematic errors in the photogrammetry approach; or (2) real changes in the shape of the surface that occurred during the measurements. We have found evidence, based on measurements made during a single night, that the surface actually changes and that these changes are due to thermally induced deformations which vary with the underlying temperatures of structural elements in the backup structure. If that is happening here, then measurement errors inferred from the difference of adjacent maps would be too large.

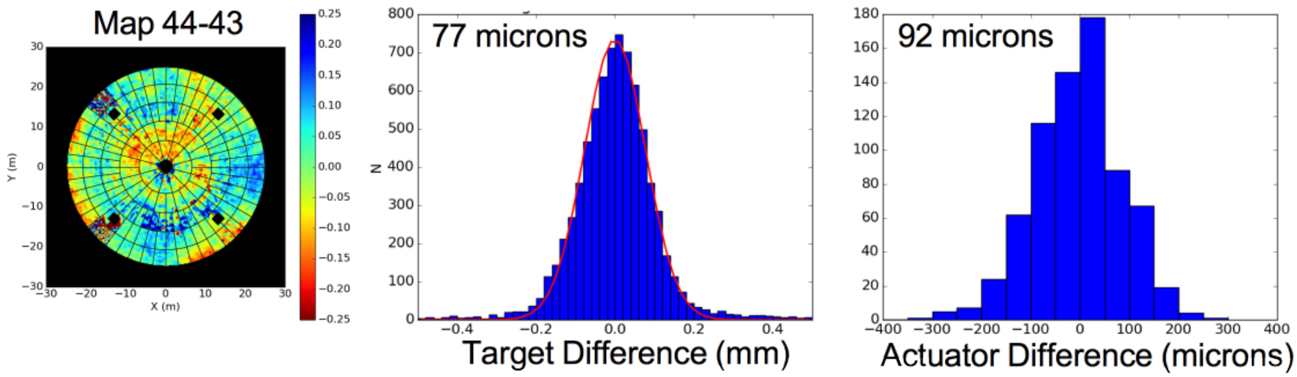

Figure 6 - Photogrammetry repeatability tests. Two maps obtained consecutively on June 4 2018 are differenced. Left image shows difference map of surface (color scale in units of millimeters); Center shows histogram of z axis differences in target positions; Right shows difference in derived actuator positions.

3.4 Fitting the Active Surface Model

The gravitational distortion of the surface leads to changes in the best actuator position with elevation angle. In order to derive a model for the motion of each actuator, we make maps at different elevations and then fit a simple quadratic model to describe the motion of the actuator. As in the analysis of a single map, the maps at each elevation are first fit to a best paraboloid, and then actuator positions are calculated with respect to the best parabolic shape for the surface at each elevation angle.

The active surface model has been derived from 9 photogrammetry maps obtained on two nights in December 2018. A log of the maps is presented in Table 1. In each case a best fitting parabola has been removed from the point cloud of the photogrammetry data and residuals to this fit along the optical (z) axis of the parabola are presented. After removal of the best parabola, the individual segments are fit to derive the best actuator positions. Table 1 presents the map rms after each of these fits.

The raw map data, after removal of the best parabola, are presented in image form in Figure 7. The images show obvious features due to individual segments in the wrong position. There are also apparent errors of low-order across the surface of the antenna. These are in part due to the surface model in use for the specific measurement, but they may also reflect changes in the shape of the surface due to thermal gradients within the backup structure.

Several segments are blacked out in the presentation of the maps. Eight segments occur at the locations where the secondary tetrapod intersect the surface. The segments at these location are shadowed by the tetrapod legs and therefore were not provided with accurate surfaces. There are also three ring 4 segments missing in the maps. These had been removed from the surface for refurbishment and replaced with temporary cover plates, as part of the ongoing program described in section 3.1.

Table 1

Night	Map	Elevation (deg)	Date	Time (local)	Z-Axis RMS Parabola Fit (microns)	Z-Axis RMS After Segment Fit (microns)
1	61	62	2018/12/13	23:19:00	138	111
1	62	80	2018/12/14	01:05:00	311	114
1	63	20	2018/12/14	02:40:00	161	99
1	64	62	2018/12/14	04:33:00	148	99
2	65	62	2018/12/14	22:25:00	144	113
2	66	40	2018/12/14	23:47:00	131	103
2	67	80	2018/12/15	01:50:00	134	109
2	68	20	2018/12/15	03:18:00	202	101
2	69	62	2018/12/15	04:55:00	134	109

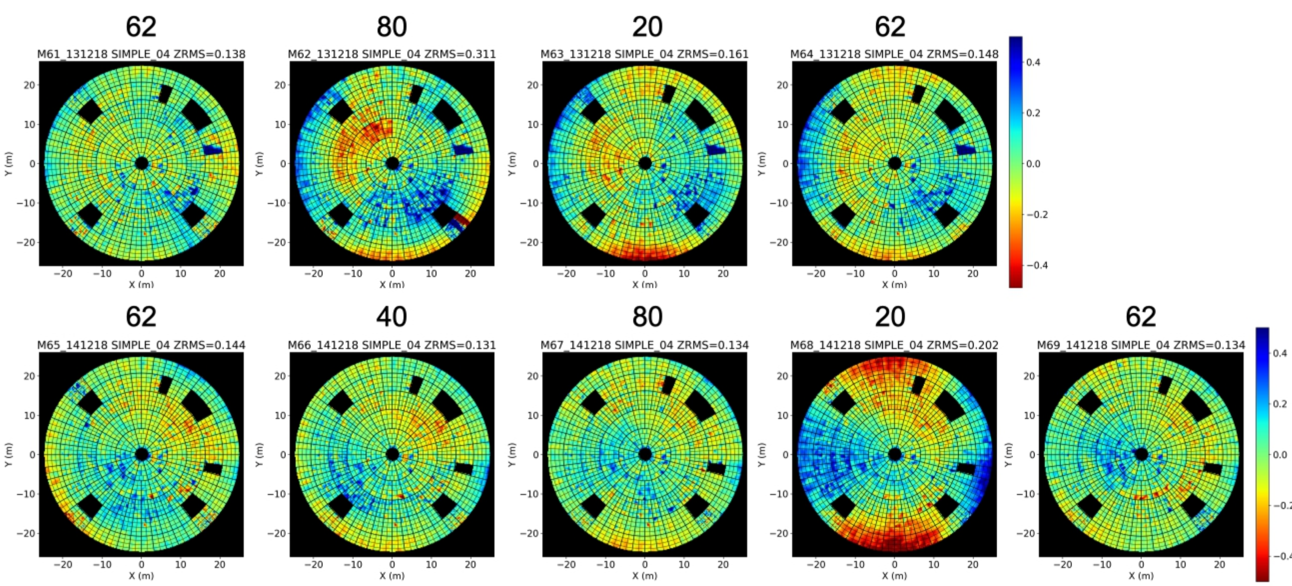

Figure 7 – Photogrammetry maps used to create the LMT active surface model. Maps were obtained over two nights. The data from the first night are shown in the first row and the data from the second night are shown on the second row. The elevation angle of the antenna is shown above each map. All maps are scaled in the same way. The color bars to the right of each row provide the scale in millimeters of deviation.

Once the maps have been used to derive the best actuator positions at each elevation, the positions are used to fit a model of the actuator position versus elevation angle. Figure 8 shows an example of the result of the fits for a single ring of the LMT, Ring 2. Ring 2 has 24 segments and therefore 96 actuators. However, gravitational deformations of the surface are left-right symmetric. Therefore, actuators at symmetric positions will counteract the same gravitational deformation with elevation, though of course there is expected to be an offset in the zero position between the two actuators in a symmetric pair. Thus, the model for each pair is constrained to have the same elevation dependent behavior for both actuators. We show figures for the 48 symmetric actuator pairs in ring 2 in the figure.

A current fit for the active surface model for each actuator pair includes 18 data points at 4 elevation angles. Figure 8 shows typical data rms with respect to the model fit of 60-70 microns in ring 2, though there are some actuators with larger errors. The rms of all data points compared to the full model is 67 microns.

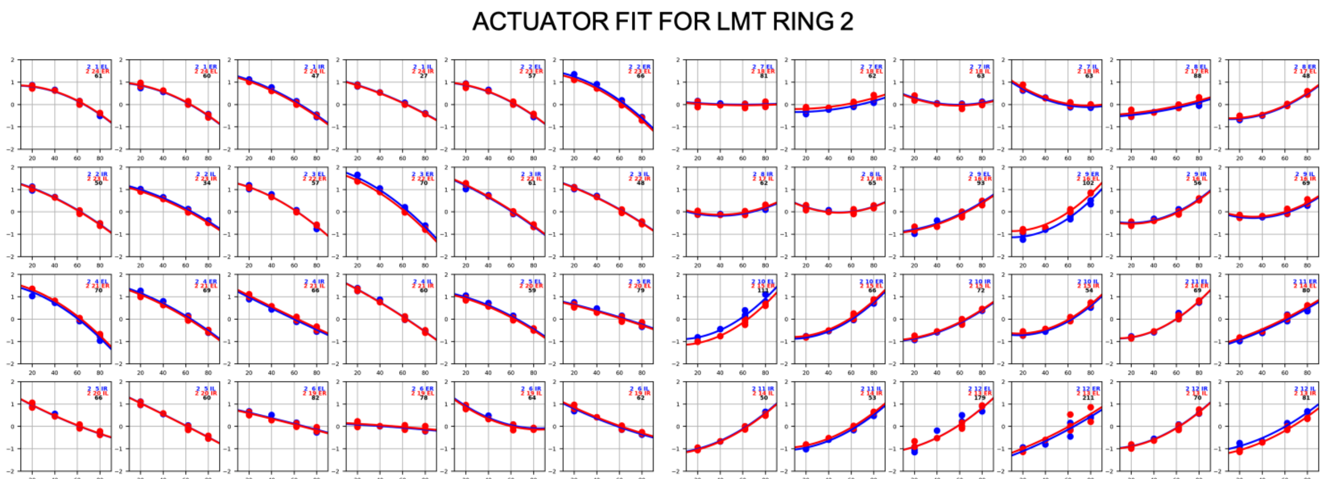

Figure 8 – Active surface model fit to all actuators in LMT Ring 2. X axis is the elevation of the actuator position measurement (degrees), and the Y axis is the actuator position in units of millimeters. There are 24 segments in Ring 2 and therefore 96 total actuators. The 48 graphs show results for the 48 pairs of actuators in left-right symmetric positions on the antenna. Each pair of actuators is fit to the same elevation-dependent model. Each graph provides the rms of the fit in units of microns.

Figure 9 shows a histogram of the rms errors for all actuator fits over all segments. There is a strong peak near the overall rms at about 67 microns. Comparison of this typical value agrees reasonably well with the actuator error of 64 microns rms estimated from the difference of two adjacent maps shown in Figure 6. However, we note that the error estimate of 64 microns assumed that all differences were only due to the measurement and fitting process. In fact, the measurements suggested that there are other causes, such as systematic changes in the shape of the antenna with time, that are also important, and so the observed residuals to the actuator model likely include these systematic errors as well.

If the rms of the actuators to the active surface fit is 67 microns, then what is the expected error in the positioning of an actuator at some specific elevation? Using a Monte Carlo simulation of the active surface model fit to actuator positions measured at the same set of elevations observed in our experiment, we find that the model's error in position over the elevation range measured will be about ½ of the actuator measurement error, corresponding to about 34 microns. A simple simulation of a segment as a thin plate with its corners positioned with random errors leads to the conclusion that the overall surface rms for the segment is about 38% of the random positions of the corners. Thus, for 67 micron rms errors of the actuator measurements and the set of elevations measured, we'd expect only a 13 micron rms error over the surface. If this is actually the case, then errors in the active surface model would contribute almost nothing to the total surface error of the antenna.

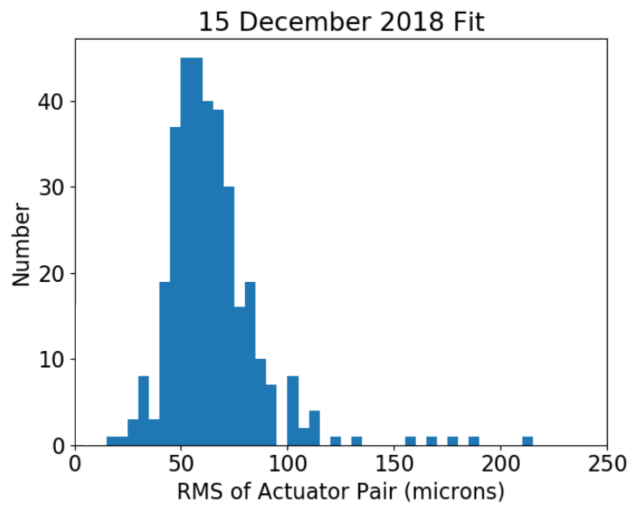

Figure 9 – Histogram of the RMS of all actuator model fits. The rms of all actuators about the best fitting model is 67 microns, which is close to the peak in the distribution.

3.5 Estimate of Internal Segment Errors

Figure 10 shows the result of averaging the residuals to about a dozen photogrammetry maps of the surface after removal of large scale deformations and segment actuator errors. There are clear residual features, representing high and low spots on the surface, that cannot be removed by setting the actuators. A histogram of these residuals is well matched by a z-axis error of 72.5 microns. This suggests a floor in our ability to set the surface with the present set of panels. Most of the worst residuals in the map have been traced to segments which still need to be upgraded (in rings 3 and 4) and to individual bad subpanels in rings 1 and 2.

The actual performance of an antenna depends on the path differences between rays which traverse the optical system and arrive at the receiver. A common way to specify path length errors due to deviations of the surface from the best parabola is to compute the "half-path" errors. For the LMT, the "half-path" rms deviation is about 80% of the "z-axis" rms deviation. A z-axis rms of 72.5 microns therefore corresponds to a half-path rms deviation of about 60 microns. Thus, if the LMT's actuators could be placed in exactly the right position, we would expect the surface to be better than its half-path specification of 75 micron rms.

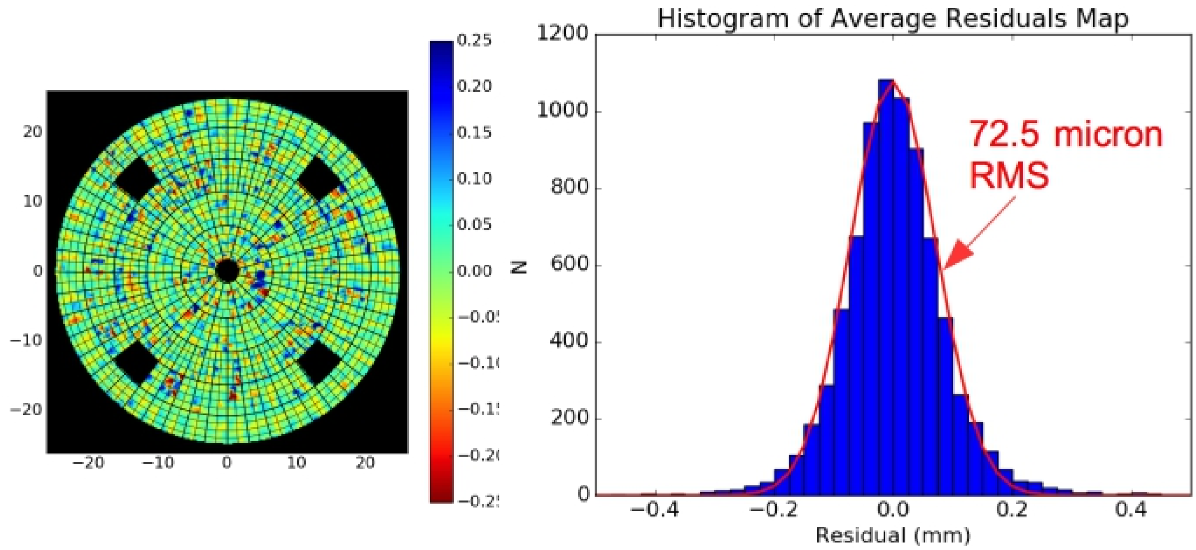

Figure 10 - Average of a number of residuals maps to search for portions of the surface which are systematically in error. Right side gives a histogram of the errors along the z-axis of the parabola.

3.6 Antenna Effective Area

We have conducted measurements of the antenna effective area in order to assess the antenna performance and estimate the total optical system rms. This requires measurements at different frequencies and requires use of different receivers to derive the surface error. Using different receivers sometimes makes the results difficult to compare, and this aspect of the work is continuing. Nevertheless, some initial conclusions have been developed and areas for further work have been identified.

According to Ruze theory, the effective area of the antenna should be a function of the frequency. The effective area, A_E, is given by:

$$A_E(\nu) = A_E(0)\ e^{-\left(\frac{4\pi\nu}{c}\epsilon\right)^2}$$

where $A_E(0)$ is the aperture efficiency at zero frequency, ε is the surface error, and υ and c are the frequency and speed of light respectively.

Our measurements involve both heterodyne receivers and the AzTEC instrument. These instruments couple to the antenna differently, and we must account for that in our analysis. For heterodyne receivers the coupling factor is about 0.8, although differences of a few percent may occur from receiver to receiver. The coupling factor for AzTEC is 0.2, which of course is quite different from the other instruments. Therefore, to place measurements with AzTEC on the same scale as measurements with the heterodyne receivers, we've corrected all measured effective areas to account for the coupling factors.

Once the coupling is removed, the main remaining factors that affect the antenna effective area are blockage losses and the loss of gain due to surface errors according to the Ruze equation above. Blockage losses include blockage by the secondary mirror supports, the central hole in the primary, the gaps between segments in the primary, and for the 50m-diameter case, an allowance for the regions around the point in the surface where the secondary supports intersect the primary mirror. The expected value for $A_E(0)$ at the LMT should be the geometrical area of the antenna less *twice* these blockage losses.

The first efforts to assess antenna effective area were made during the Early Science campaigns when the instruments only illuminated the inner 32m-diameter of the primary mirror. These observations are shown in Figure 11 as blue points. Measurements were made using the Redshift Search Receiver and the AzTeC instrument initially and then supplemented with a measurement at 1.3mm wavelength during the 2017 observational campaign of the Event Horizon Telescope. Plotting all three points along with the Ruze Theory curve originally fit to the RSR and AzTEC data suggest that the surface is consistent with an overall system optical rms of about 85 microns. The value of $A_E(0)$ is 69% of the geometrical area of the 32m-diameter antenna,whereas the expected value based on blockages would be 90%. Thus, the observed value is somewhat problematic because it would suggest an *additional* 20% losses on top of the expected blockage losses.

Figure 11 also shows more recent results of measurements of the effective area of the 50m-diameter antenna made with the RSR, the SEQUOIA focal plane array, the new 1mm SIS receiver, and a 2mm receiver(B4R) provided by colleagues at the NAOJ. Effective area has again been corrected for receiver coupling (assuming a value of 0.8) to make it consistent with the 32m-diameter data. Measurements in the 3mm window were carried out in June 2018 after the initial setting of the 50m-diameter antenna. Points are shown for several measurements using the RSR (shown in black) and two measurements using SEQUOIA (shown in red). There are differences of a few percent in the results, but this is probably within the likely differences in coupling of these receivers to the antenna. The 1.3 mm measurement was made following the more detailed fit of the antenna surface described in the previous section. This led to an improvement in the effective area at 1.3mm, but that should not have had a strong effect on the 3mm measurements so we feel justified in using the 3mm points and the 1.3mm points together in this initial analysis.

The Ruze theory curve going through the 50m-diameter LMT points uses a surface error of 98 microns rms. We expect the intercept at zero frequency to occur at 85% of the geometrical area of the 50m antenna based on detailed calculations of the blockage and an allowance for the segments adjacent to the secondary support legs in ring 4.   This time, the model shown finds that $A_E(0)$ = 80% for that parameter which we note is in better agreement with expectations than the result for the 32m-diameter dish.

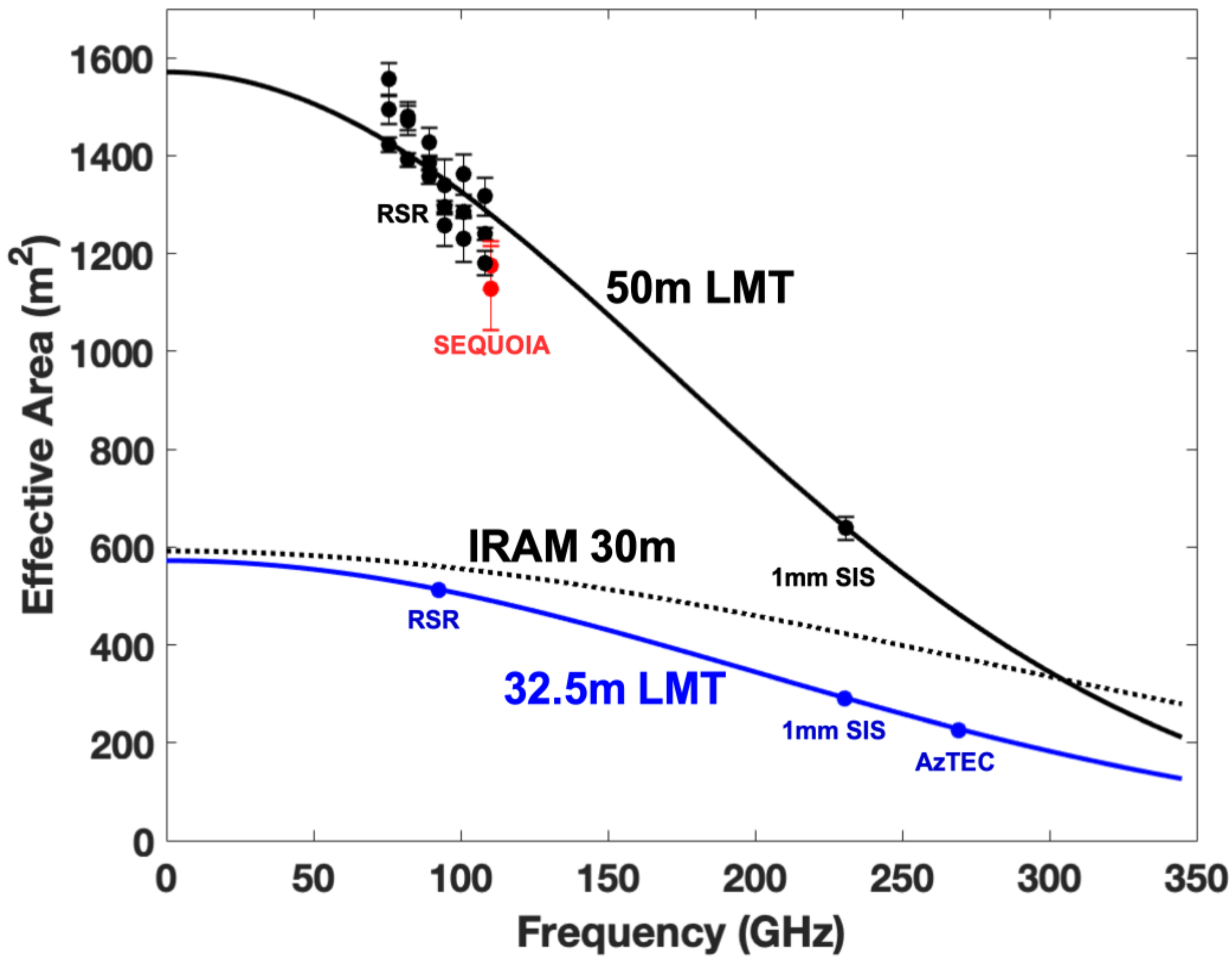

Figure 11 – Measurements of the Effective Area of the LMT versus frequency. Measurements are shown for the "Early Science" 32.5m-diameter dish (in blue) and for the 50m-diameter dish (in black and red). Effective areas have all been presented with a correction for antenna coupling in order to allow a measurement by the AzTEC instrument to be compared to the other LMT instruments. A Ruze Theory model is presented for each case. The 32.5m-diameter model has an effective area at zero frequency of 69% of geometric area and a surface rms of 85 microns. The 50m-diameter model has a zero frequency effective area of 80% of geometric area and a surface rms of 98 microns. The dotted line shows the effective area of the IRAM 30m telescope assuming parameters published in the IRAM Annual Report of 2007 with a coupling correction of 80% applied.

A few conclusions are apparent from consideration of Figure 11:

1. The expansion of the surface from the 32m-diameter dish to the 50m-diameter dish had the expected effect on the effective area of the antenna. Figure 12 confirms this result with an actual observation at 3mm wavelength of the same source with the RSR before (red) and after (blue) the increase in the antenna area.

2. The intercept, $A_E(0)$, for the 50m-diameter antenna is higher than that found for the 32m-diameter antenna. The reason for this is under investigation, but we do note that the surface accuracy of the new secondary mirror provided for the 50m antenna is a significant improvement over the initial secondary used at the LMT.

3. The surface errors on the 50m-diameter dish do not seem to be quite as good as those obtained using only the inner 32m-diameter. Based on photogrammetry data used to set the dish, we might have expected to do better. The value from the Ruze theory fit of 98 microns rms would be the equivalent to a z-axis rms in the photogrammetry data of about 122 microns rms. This value for z-axis errors falls just below that observed in the maps (approximately 140 microns rms, see Table 1) that went into the active surface model determination. We might have hoped to see errors closer to those found after fitting for best actuator positions in each map according to Table 1: 100-110 microns along the z-axis, corresponding to 80-88 microns for the half-path rms. It appears, therefore, that there is still a need to continue alignment work on the 50m-diameter antenna in order for the LMT to achieve its full sensitivity.

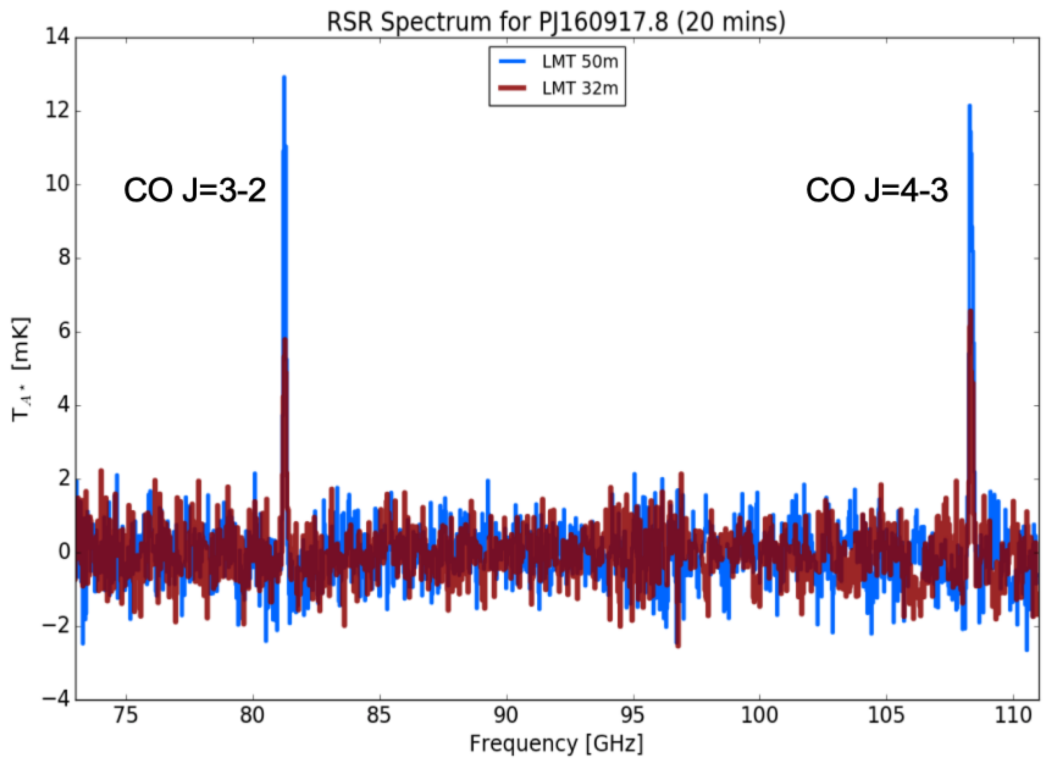

Figure 12 – Observations of the submillimeter galaxy PJ160917.8 made with the Redshift Search Receiver. Measurements made before the upgrade to the full 50m antenna are shown in red. Measurements made after the upgrade are shown in blue. The improvement in the signal level is reasonably consistent with the measured gain in antenna effective surface area.

3.7 Future Work: Impact of Thermal Deformations

In view of the discrepancy between the expectations for the surface rms from photogrammetry maps and the measurements of antenna effective area, it is important to consider why better results were not achieved. One potential problem with the setting of the antenna is the assumption that all the maps going into the active surface model are only influenced by gravitational distortions. However, we know that thermal distortions are likely to be important as well, based on tests like those illustrated in Figure 6. As a further example, Figure 13 shows a sequence of photogrammetry maps obtained on the same night. The actuator positions were updated after each map, and so ideally the surface should have improved with each iteration. Instead, we note that significant systematic residuals remained. It is clear that there is some underlying, low order, surface deformation occurring during the night, which we attribute to thermal deformations.

Trying to set the antenna in the presence of thermal deformations is very problematic since we must not confuse permanent setting errors with transient thermal errors. The best results will be found if we limit the surface measurements to those times after midnight when the antenna's temperature has, more or less, equilibrated. This is mostly the case for the set of maps used to derive the active surface model, but perhaps there is enough variation during the two nights of observation to affect the active surface model fit.

Most large radio telescope antennas make use of active systems to try to control thermal gradients within the structure, but so far the LMT has only passive measures (i.e. thermal cladding of the backup structure) in place. A project to add active measures, including continuous circulation of air within the backup structure, is underway at this time.

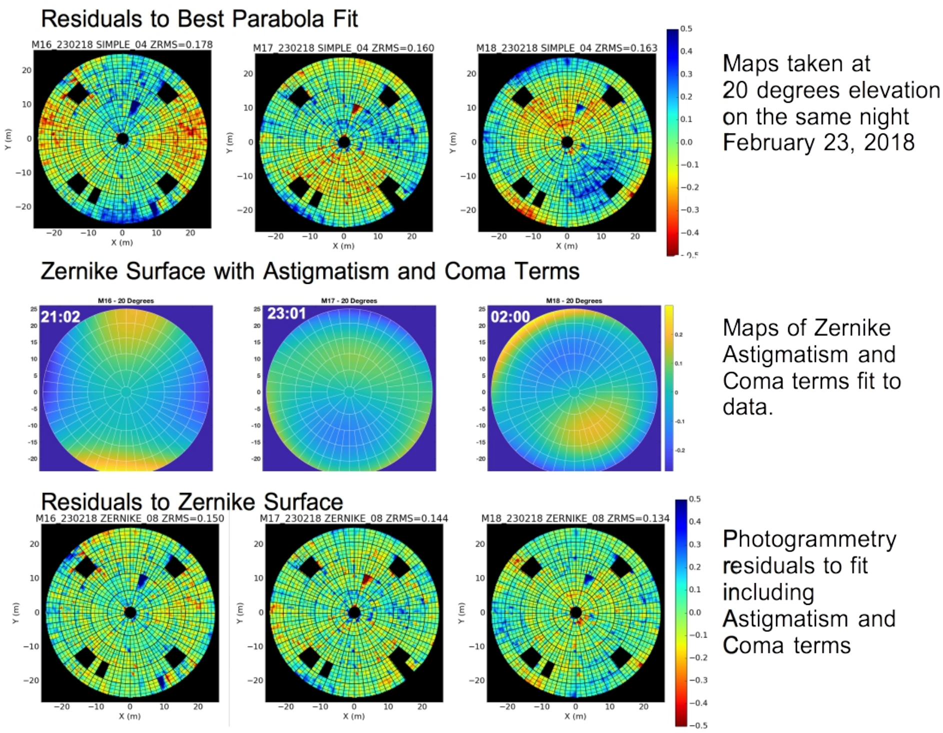

Figure 13 - Example of probable thermal deformation errors on the antenna. Data were obtained at 20 degrees elevation on a single night between 9 pm and 2 am. The top row shows the maps with the best fit parabola removed. The middle row shows the result of a low order fit to the residuals including coma and astigmatism terms. The bottom row shows the residuals after removal of the coma and astigmatism terms.

4. ANTENNA POINTING

The pointing of LMT has always been considered to be one of its greatest technical challenges. The LMT's official pointing specification is given in terms of the ability of the antenna to move to a target source from a pointing calibration source located within ~10 degrees of the target. This “offset pointing” specification calls for the antenna to move from the calibration source to target source within 1” or better.

The development of the complete antenna pointing model for the LMT is still underway as we identify new factors which can affect the pointing. The initial step was fitting a standard antenna pointing model (the Stumpf model) which considers misalignments of the antenna structure. Such a model was successfully used for all observations obtained during the 32m-diameter Early Science period. The LMT's basic pointing model follows those in use at many radio telescopes. Figure 14 shows the results of such a model fit using data from a recent pointing campaign with the SEQUOIA instrument on the 50m-diameter antenna. When small night-to-night drifts are accounted for, the typical all-sky pointing rms is 2”. Offset pointing to target objects from nearby calibrators is typically much better at the desired level of about 1”.

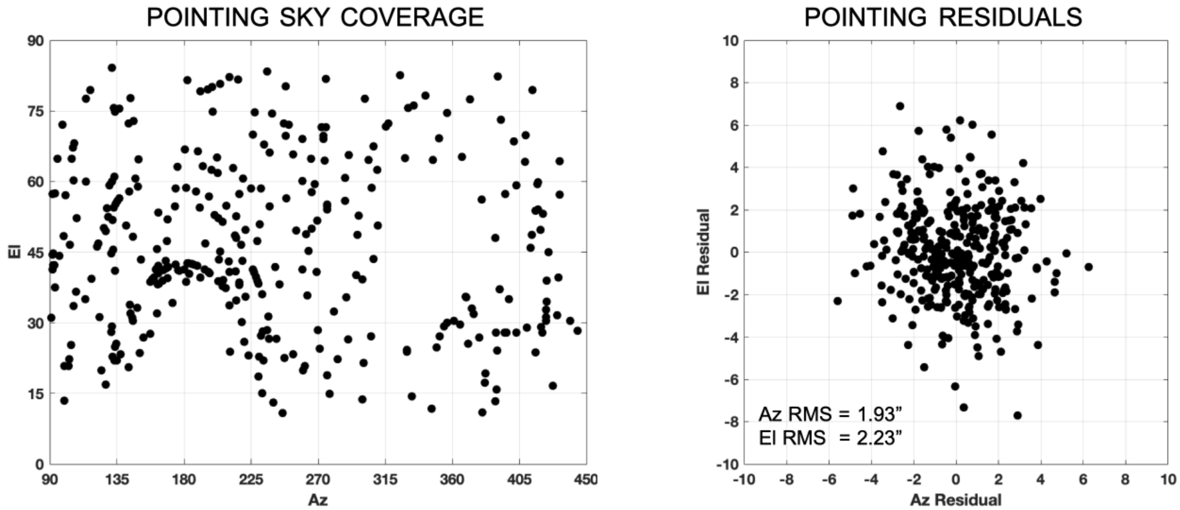

Figure 14 – Results of the fall 2018 pointing campaign at the LMT. The left panel shows the data distribution on the sky. The right panel shows the residuals to the all-sky fit to the pointing model.

The pursuit of even better pointing of the antenna is underway. Measurements have shown the effects of unevenness of the LMT's azimuth track are an important contributor to pointing errors. Figure 15 shows average values of the azimuth and elevation pointing errors, after removal of the basic pointing model, for different azimuth positions of the telescope. The data are taken from observations made during a previous pointing campaign in 2015. Measurements show the same behavior with two different receivers and are consistent with azimuth track errors. The effect is obviously important at the level of 1-2” and it will be included in the full pointing model in a future campaign.

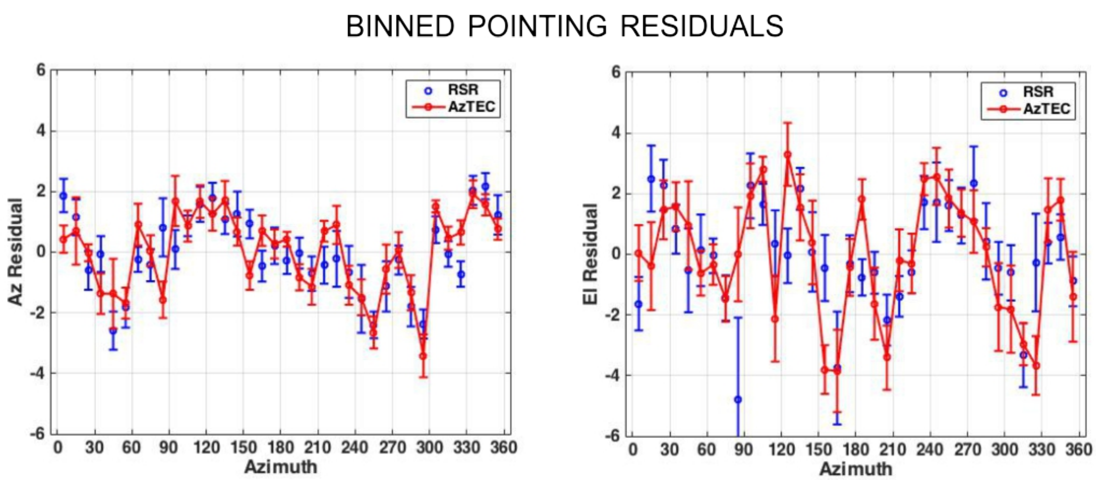

Figure 15 – Residuals to pointing models averaged in bins of the antenna azimuth position. The left panel shows the average residual in azimuth and the right panel shows the average residual in elevation. The blue points show RSR measurements and the red points are data taken with the AzTEC instrument. The average values for both RSR and AzTEC are consistent and show systematic trends at the level of 2”. The form of the variations is consistent with expectations for errors due to unevenness in the azimuth track.

5. EXAMPLES OF INSTRUMENT PERFORMANCE

5.1 Early Science Results with First-light Facility Instruments (2013-2017)

The first instruments installed on the LMT for Easrly Science demonstrations were the Redshift Search Receiver and the AzTEC camera. The RSR is an ultra wideband (74-111 GHz) receiver/spectrometer for the 3mm wavelength atmospheric window. Its primary function is to allow for blind searches of spectral lines in distant objects in order to determine redshifts. AzTEC is a 144-pixel continuum camera system operating at 1.1 mm wavelength. In addition to RSR and AzTEC, a special purpose 1.3mm SIS receiver was commissioned for Very Long Baseline Interferometric observations with the Event Horizon Telescope in 2017. We present a few examples of the Early Science results in the following sections.

5.1.1 RSR Observations

Since their discovery, submillimeter-selected galaxies (SMG's) have revolutionized the field of galaxy formation and evolution. The LMT's Redshift Search Receiver was designed and constructed to allow the determination of spectroscopic redshifts from SMGs found in continuum surveys of the sky. Figure 16 shows a set of spectra, mostly from the work of Harrington et al (2016), that illustrate the use of the RSR for redshift measurements.

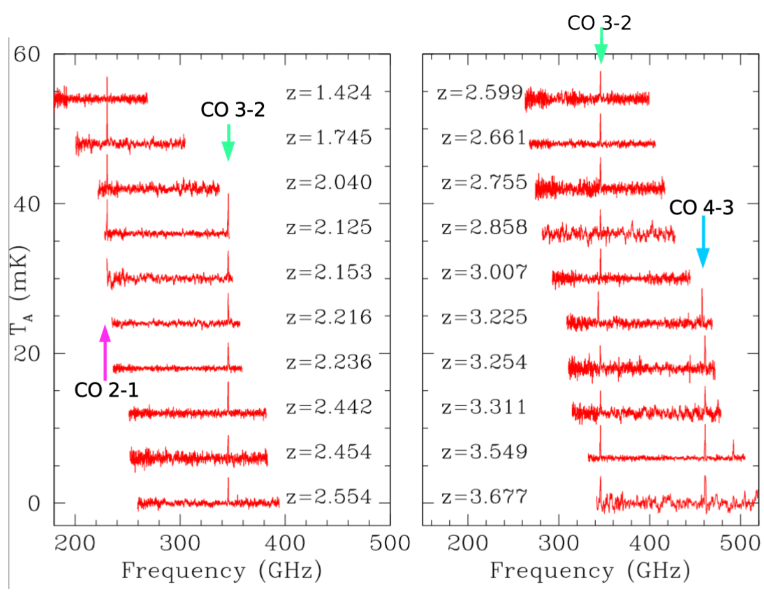

Figure 16 – RSR Spectra of a set of 20 submillimeter galaxies. The spectra are plotted against the rest frequency of the lines so that the different CO lines observed line up at the same frequency. The redshift is given for each spectrum.

Of all submillimeter galaxies that have been discovered, only a handful of sources have been confirmed to lie at z > 5 and only two at z ≥ 6. All of these are rare examples of extreme, optically obscured, starburst galaxies with star formation rates of ≳1,000 $M_\odot$ yr^{-1} and therefore are not representative of the general population of dusty star-forming galaxies. Consequently, our understanding of the nature of these sources, at the earliest epochs, is still incomplete. The recent detection of a dusty star-forming galaxy at z = 6.027 by Zavala et al (2018) is an important advance in this field. After correcting for gravitational lensing, the derived star formation rate and gas and dust properties are similar to those measured for local ultra luminous infrared galaxies, extending the local trends to a poorly explored territory in the early Universe. Figure 17 shows the detections of CO and water lines in the source, made with the RSR at the LMT, as well as an additional measurement of CII conducted with the Submillimeter Array (SMA).

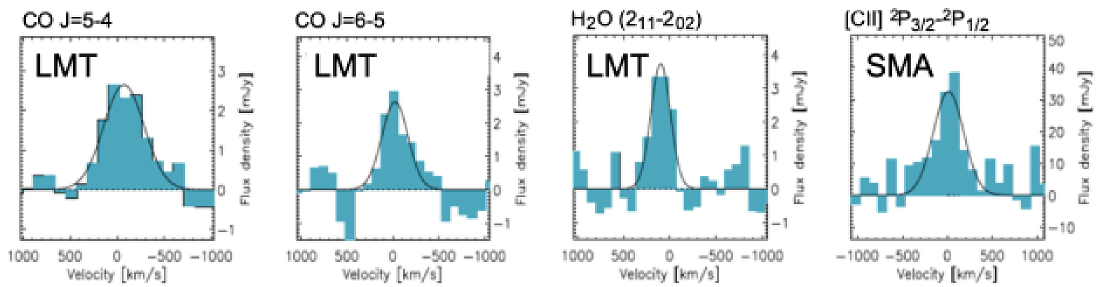

Figure 17 - Spectral lines of CO and water observed with the LMT/RSR in the dusty starforming galaxy G09.83808 at redshift of 6.0269 (Zavala et al 2018). A measurement of the [CII] $^2P_{3/2}$-$^2P_{1/2}$ line, obtained with the Submillimeter Array (SMA), is also shown.

5.1.2 AzTEC Observations

∊ Eridani is a nearby, young Sun-like star that hosts a ring of cool debris analogous to the Solar system's Edgeworth-Kuiper belt. Early observations at (sub-)mm wavelengths gave tentative evidence of the presence of inhomogeneities in the ring, which have been ascribed to the effect of a putative low eccentricity planet, orbiting close to the ring. The existence of these structures has been recently challenged by high-resolution interferometric millimetre observations. Observations made with AzTEC on the LMT (Chavez-Dagostino et al 2016) resulted in the deepest single-dish image of ∊ Eridani at millimetre wavelengths. The main goal of these LMT observations was to confirm (or refute) the presence of non-axisymmetric structure in the disc. The dusty ring was detected for the first time along its full projected elliptical shape. The radial extent of the ring is not spatially resolved and shows no evidence, to within the uncertainties, of dust density enhancements. Additional features of the 1.1 mm map are: (I) the presence of significant flux in the gap between the ring and the star, probably providing the first exo-solar evidence of Poynting-Robertson drag, (II) an unambiguous detection of emission at the stellar position with a flux significantly above that expected from ∊ Eridani's photosphere, and (III) the identification of numerous unresolved sources which could correspond to high-redshift background dusty star-forming galaxies.

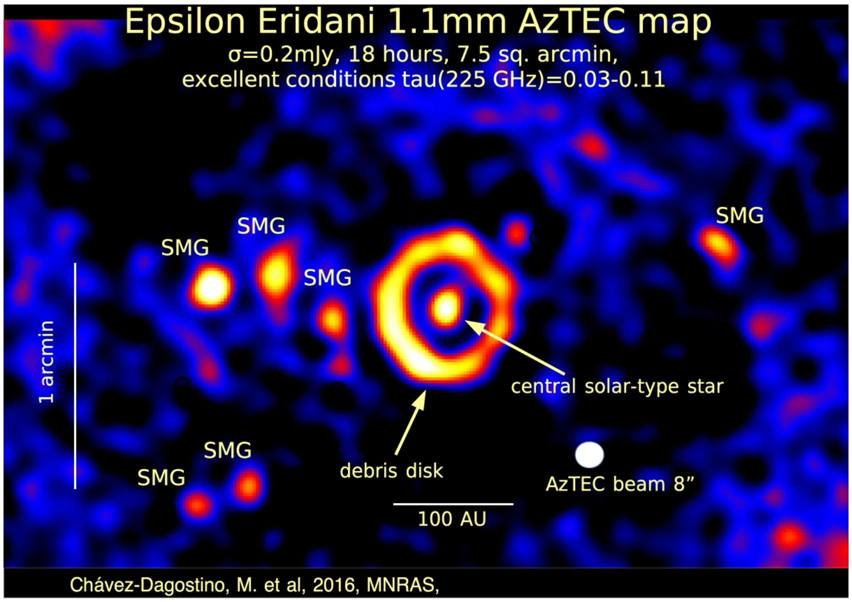

Figure 18 – LMT/AzTEC image of the dusty debris disk surrounding the star Epsilon Eridani (Chavez-Dagostino et al 2016). Emission from dust near the central star is also apparent. The image background also contains a number of submillimeter galaxies (SMG).

Heyer etal (2018) used the AzTEC camera on the LMT to image the 1.1mm dust continuum emission over a 1 square degree area within the Galactic Plane centered on the coordinate l,b=24.5,0 to a point source sensitivity of 10 mJy within an 8.5 arcsec beam. Over 1500 compact sources were identified and distributed over distances of 2 to 12 kpc. Many of these AzTEC sources are related to the large, massive clumps identified in the Bolocam Galactic Plane Survey (BGPS) with a lower angular resolution of 35 arcsec. The individual AzTEC sources are fragments within these massive clumps and comprise 5-15% of the clump mass. For clumps with established gas temperatures and distances less than 5.5 kpc at which the Jeans' length is resolved by the LMT, the AzTEC masses are consistent with Jeans' gravitational instability.

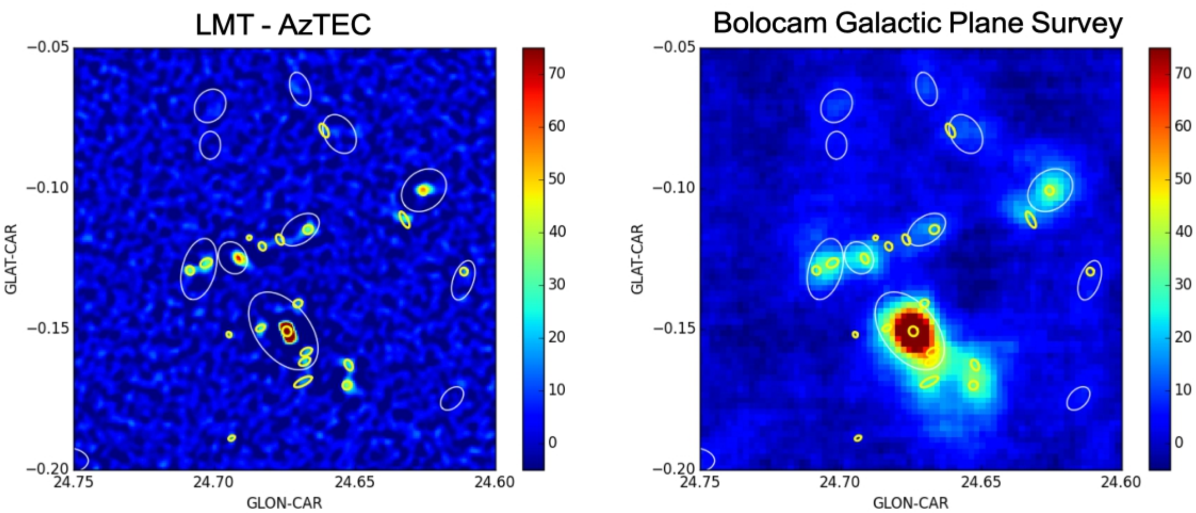

Figure 19 – Maps of a 9'x9' region obtained by 32m-LMT/AzTEC (left) and Bolocam/CSO (right). The high (8”) resolution LMT/AzTEC maps resolve sources within those identified with the lower resolution Bolocam/CSO maps. Contours highlight the AzTEC sources.

5.1.3 Very Long Baseline Interferometry (VLBI)

Interest in using the LMT as a station for millimeter-wave Very Long Baseline Interferometer experiments, particularly those addressing the study of supermassive black holes, led to the installation of a hydrogen maser frequency standard, VLBI recording equipment, and receivers for the 1.3mm atmospheric window.

The radio emission from Sgr A* is thought to be powered by accretion onto a supermassive black hole of˜ $4\times10^6\ M_\odot$ at the Galactic Center. At millimeter wavelengths, Very Long Baseline Interferometry (VLBI) observations can directly resolve the bright innermost accretion region of Sgr A*. The first VLBI observations with the LMT were carried out with the US Very Long Baseline Array (VLBA). Ortiz-Leon et al (2016) successfully detected Sgr A* at 3.5 mm with an array consisting of six VLBA telescopes and the LMT. The source was modelled as an elliptical Gaussian brightness distribution to estimate the scattered size and orientation of the source from closure amplitude and self-calibration analysis. The intrinsic two-dimensional source size at 3.5 mm is 147+/- 7 µarcsec × 120+/- 12 µarcsec with a position angle 88 +/- 7degrees east of north.

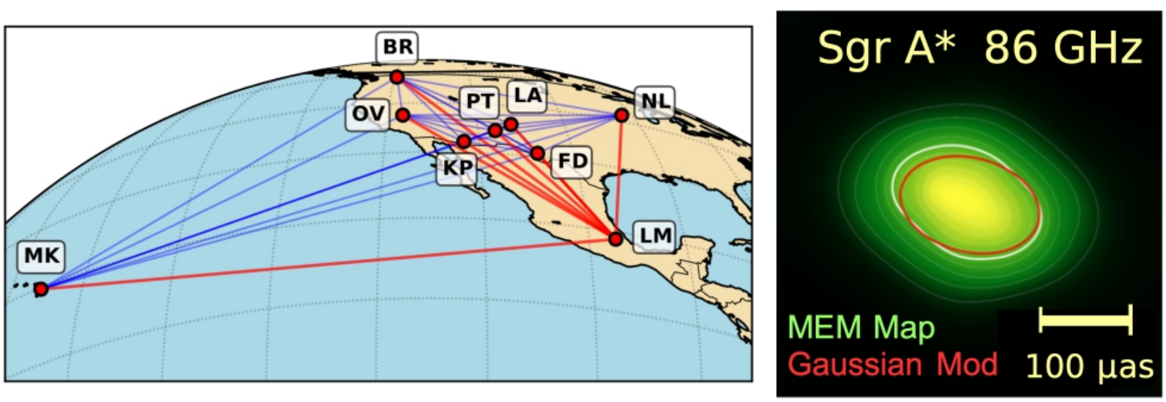

Figure 20 – 3mm VLBI observations of SGR A (right) made with the LMT and the VLBA (left). The observations were able to resolve the central radio source and measure its north-south extent for the first time, due to the southerly location of the LMT relative to the VLBA (Ortiz-Leon et al 2016)*

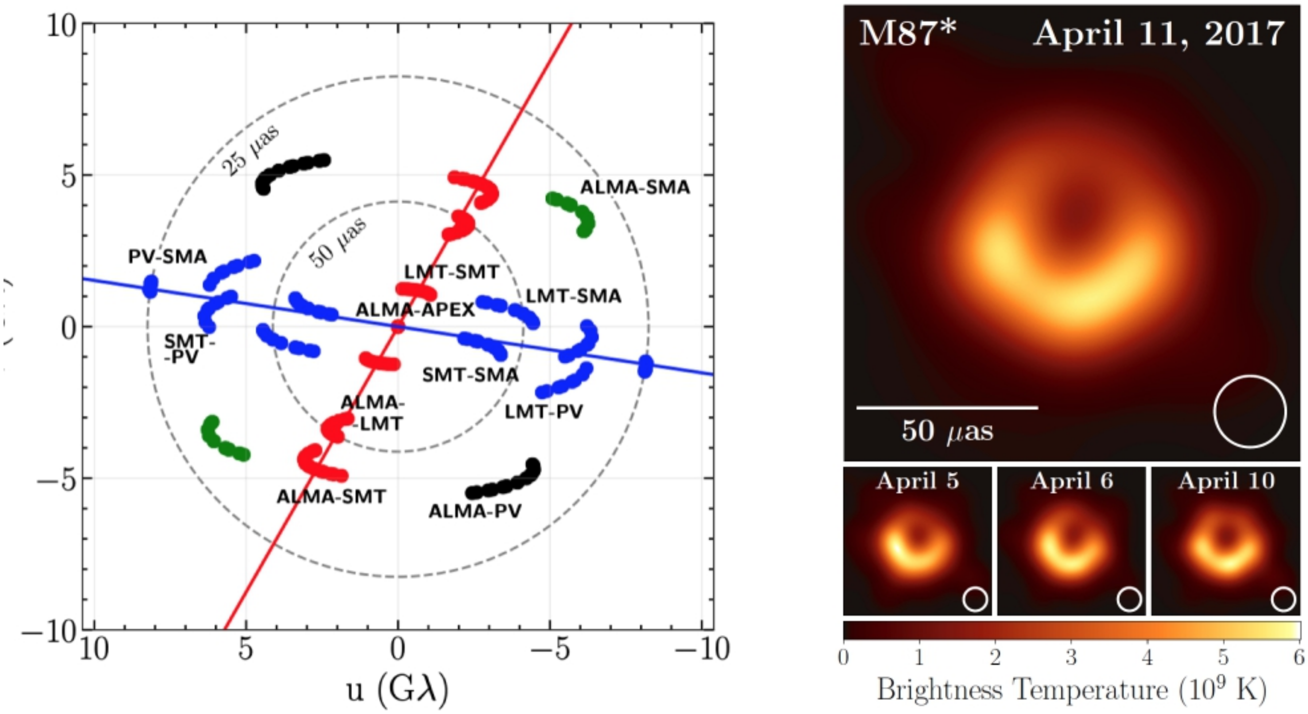

Figure 21 – Results of the Event Horizon Telescope campaign to image the central black hole in M87. The left hand panel shows the U-V coverage for the VLBI observations. Baselines involving the LMT fill important areas on the U-V plane. The LMT's large collecting area and its location in the array make it an important contributor to the experiment. The right hand panel shows the resulting image of the shadow of a supermassive black hole silhouetted by the hot plasma rotating around the singularity at relativistic velocities (EHT Collaboration 2019).

When surrounded by a transparent emission region, black holes are expected to reveal a dark shadow caused by gravitational light bending and photon capture at the event horizon. The LMT is an important part of the Event Horizon Telescope, a global VLBI array which has been organized to study this phenomenon. The first observations to reconstruct event-horizon-scale images of a supermassive black hole were publicly reported on April 10, 2019. The bright radio source at the location of a candidate black hole in the center of the giant elliptical galaxy M87 was resolved and shown to be an asymmetric bright emission ring with a diameter of 42 ± 3 μas.,The observed image is consistent with expectations for the shadow of a Kerr black hole as predicted by general relativity. The asymmetry in brightness in the ring can be explained in terms of relativistic beaming of the emission from a plasma rotating close to the speed of light around a black hole. Analysis of the images derives a central mass of $M = (6.5 \pm 0.7) \times 10^9 M_{\odot}$. These observations thus provide powerful evidence for the presence of supermassive black holes in centers of galaxies and as the central engines of active galactic nuclei. They also present a new tool to explore gravity in its most extreme limit and on a mass scale that was so far not accessible.

5.2 New Instruments

During the spring of 2018, three new instruments were installed at the LMT: (1) SEQUOIA, a 16-element focal plane array for the 85-115 GHz frequency window;

(2) a 210-270 GHz, dual polarization, sideband separating, SIS receiver; and (3) an SIS receiver covering ALMA Band 4 (2mm window). All the new receivers are still undergoing commissioning testing. We describe below a series of early observations that have been performed with the SEQUOIA instrument to establish its "mapping speed" and characterize its performance.

Figure 22 shows the maps of the inner part of the Orion Molecular Cloud obtained in the HCN J=1-0, HCO^+ J=1-0, and N_2H^+ J=1-0 lines. The LMT/SEQUOIA maps of the peak intensity of the lines, shown in the Figure, agree well with similar maps made with other telescopes.

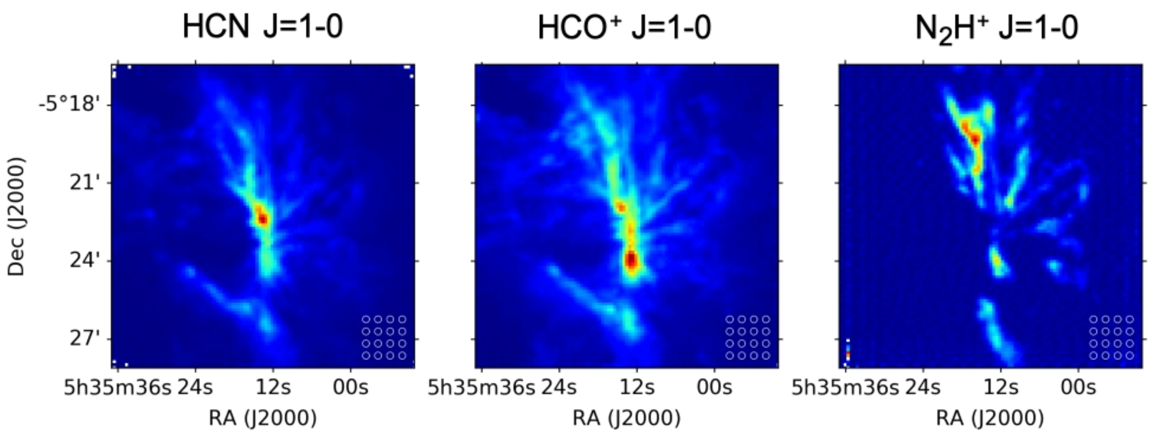

Figure 22 - Maps of the central portion of the Orion Molecular Cloud in different molecular lines. The footprint of the SEQUOIA array is shown in the lower right corner of each map.

Four on-the-fly (OTF) maps were made of a 600"x600" region surrounding the position of the well studied carbon star IRC+10216. The result of averaging all 4 maps is shown in Figure 23.

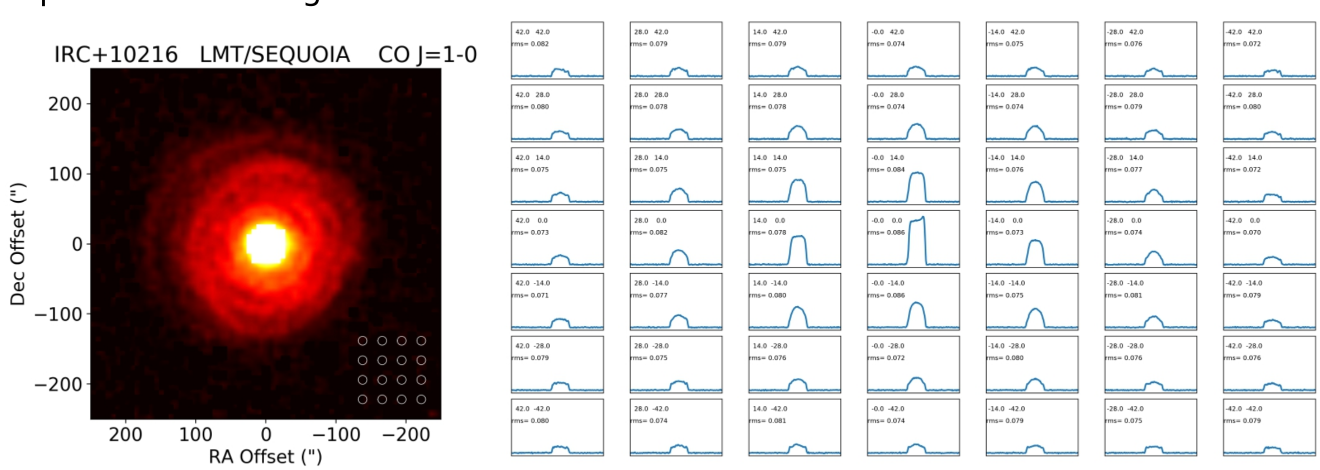

Figure 23 – Result of averaging 4 OTF maps of the CO J=1-0 line in the region around the carbon star IRC+10216. The left hand panel shows an image of the emission near the line center. The envelope around the star shows evidence of multiple shells, as seen previously in IRAM 30m maps of the CO J=2-1 emission made at approximately the same angular resolution. The footprint of the SEQUOIA array is shown in the lower right corner of the image. The right hand panel shows the spectra collected towards the inner part of the image on a 14" grid.

Finally, nine 240"x240" maps were obtained on a blank sky region at the 115 GHz frequency of the CO J=1-0 line. The results of averaging the nine maps together is shown in Figure 24.

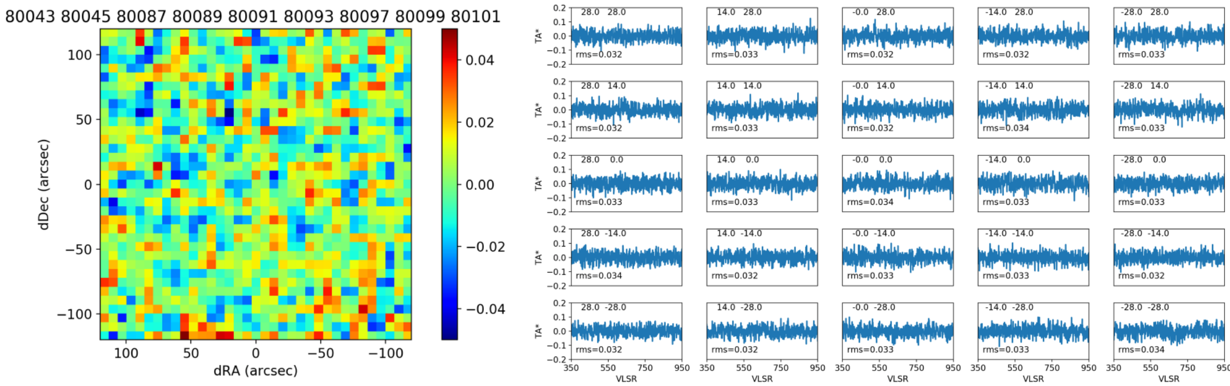

Figure 24 – Blank Sky mapping test results at 115 GHz. The left panel shows an OTF map of a single 1 km/s channel created by averaging 9 OTF maps of a 240X240 arcsec area. This required a total amount of telescope time, including all overhead involved in moving the antenna, of 5940 seconds to collect the data for the map. The rms is approximately 33 mK. The right panel shows the spectra from the inner part of the map at a resolution of 391 kHz, which would correspond to 1 km/s. Smoothing spectra to lower spectral resolution yields lower rms in proportion to inverse square root of the bandwidth.

Taken together, this set of maps allows a determination of the mapping speed of the SEQUOIA array as well as tests to demonstrate that the sensitivity of map can be improved by averaging a number of maps. Figure 25 illustrates the latter point for the blank sky tests, where we have computed the rms in combinations of 1, 2, 4, and 9 maps and shown that it follows the expected behavior.

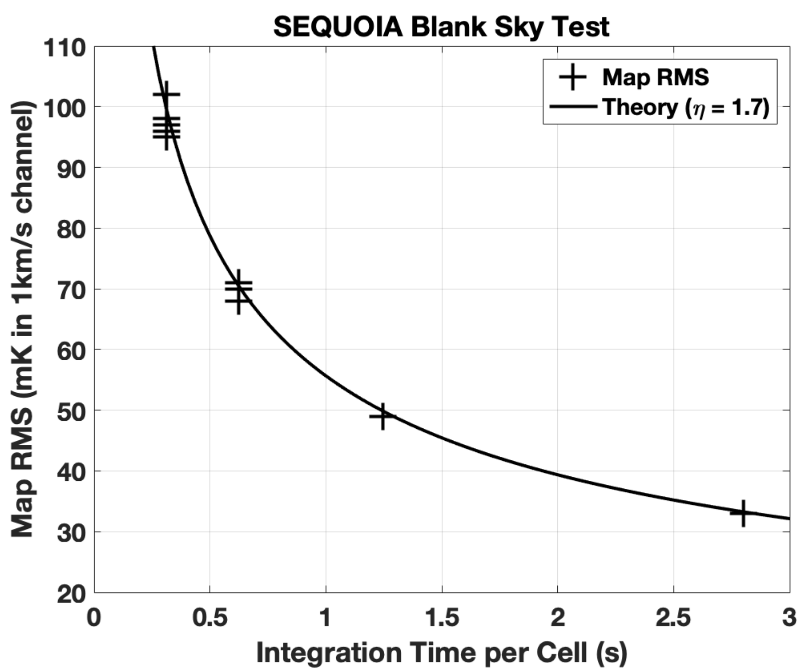

Figure 25 – RMS achieved by averaging OTF maps together in the "blank sky" experiment. Integration time per cell is about .3 s in the individual maps and grows as a number of maps are averaged. In this case we show the results for averages of 4 pairs of maps (0.6s) and 2 sets of four maps (1.2s). We also show the final result of averaging all 9 maps obtained in the experiment. The theoretical curve assumes a value of η=1.7 found through analysis of the blank field data and shows that the noise integrates down inversely proportional to the square root of the integration time.

Figure 26 shows a calculation of the expected rms in a spectral channel for a given total amount of telescope time, which *includes* the measured overhead of moving the telescope to make the map, as a function of the area being mapped. The diagonal lines show the relationship between the depth of the map and the size of the map in a given amount of telescope time devoted to a particular project. For each line we consider a case with a specific spectral resolution and a fixed amount of observing time. All parameters used in the calculation are summarized in Table 2. It should be especially noted that the antenna temperatures shown are "main beam" brightness temperatures, which are achieved by dividing the raw chopper wheel temperatures (T_A*) by the beam efficiency of 0.65. The spectral resolutions considered are: 0.05 km/s, 1 km/s, and 5 km/s. We consider total telescope times of 1, 10, and 100 hours.

TABLE 2

Parameter	Value
Frequency	100 GHz
System Temperature	100 K
Beam Efficiency	0.65
Scan Rate	30 "/s
Nyquist Cell Size	7"
Row Spacing/Cell Size	0.9
Convolution Factor (η)	1.5
total elapsed time / scan time	1.6

To establish a benchmark for the LMT/SEQUOIA calculation, we compare our predictions in Figure 26 to the same quantities computed for ALMA in order to demonstrate the ability of SEQUOIA to carry out state-of-the-art mapping programs. In order to make such comparative plots, we have proceeded in the most straightforward way. We use the ALMA cycle 6 sensitivity calculators adopting a spectral resolution of 1 km/s at a frequency of 100 GHz in order to estimate the brightness temperature rms for the ALMA 12m telescope array and the ACA array given the largest possible synthesized beam for each case (5" and 12" respectively). The choice to use the largest beam allows a more consistent comparison to the LMT beam at 3mm wavelength of about 15". The total time allowed for the experiment is divided into a number of fields to be observed and then the sensitivity calculator is used to estimate the rms. However, in so doing, there is no accounting for any overhead in the timing of the ALMA observations, which is something we explicitly account for in the LMT calculation. The example points (black and white) shown in Figure 5 were selected to give about 25 mK rms in a 1 km/s channel in a one-hour observation to cover the entire field.

Another way to benchmark the LMT results is to look at surveys made with ALMA. In this case we make use of results reported in the PHANGS survey of galaxies (Sun et al 2018). In this case, the maps were made with ~1" angular resolution and 2.5 km/s spectral resolution. The points in Figure 26, shown in red, illustrate the consequence, in terms of map sensitivity, of going to higher angular resolution. Smoothing to lower angular resolution would achieve lower rms, but the value of doing that depends on the ability of the interferometer to be equally sensitive to all spatial scales in the map.

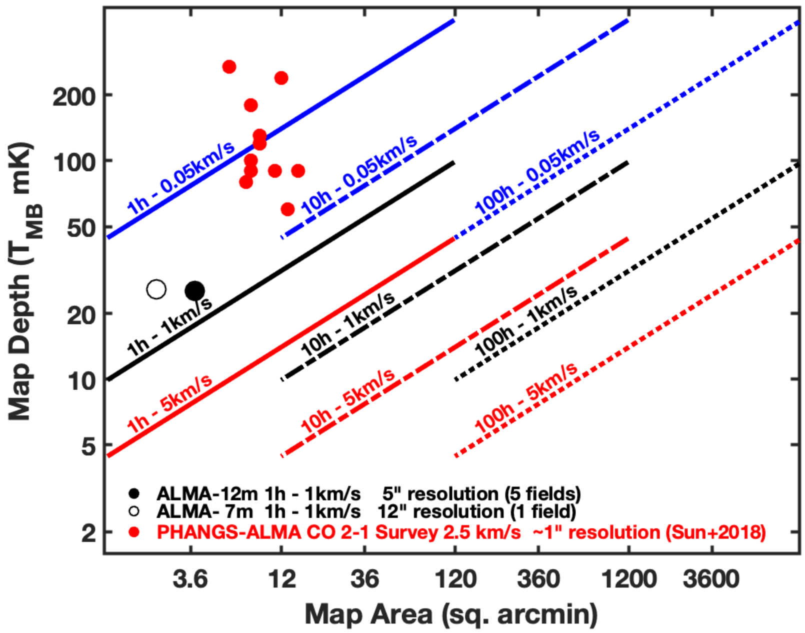

Figure 26 - Mapping speed calculations for SEQUOIA focal plane array on the 50m-diameter LMT compared to possible surveys with ALMA. The map speed for the SEQUOIA focal plane array is based on actual performance achieved during commissioning tests. Each curve notes total required telescope time and spectral resolution. ALMA points (black) are based on Cycle 6 sensitivity calculator for 1h of integration time. Red points are map results from PHANGS-ALMA survey (Sun et al. 2018). All map depths are given at the 1-sigma level.

6. SUMMARY

The LMT Collaboration is prepared to offer LMT access to the US community, pending funding from the US Government to cover a share of the cost of telescope operation and scientific support for US Community users. The 50m-diameter Large Millimeter Telescope Alfonso Serrano has been completed and outfitted with a powerful set of scientific instruments that span the 3mm to 1mm atmospheric windows. Commissioning results show that the antenna is well characterized and that an important understanding of its active surface, antenna pointing, and instrumentation has been developed. The next steps for the LMT Project are to press ahead with optimization of the antenna surface and extension of the teescope's operational hours into the daytime, in order to gain more observing time for our user community..

References

Chavez-Dagostino, M.; Bertone, E.; Cruz-Saenz de Miera, F.; Marshall, J. P.; Wilson, G. W.; Sánchez-Argüelles, D.; Hughes, D. H.; Kennedy, G.; Vega, O.; De la Luz, V.; Dent, W. R. F.; Eiroa, C.; Gómez-Ruiz, A. I.; Greaves, J. S.; Lizano, S.; López-Valdivia, R.; Mamajek, E.; Montaña, A.; Olmedo, M.; Rodríguez-Montoya, I. Schloerb, F. P.; Yun, Min S.; Zavala, J. A.; Zeballos, M., *Early science with the Large Millimetre Telescope: Deep LMT/AzTEC millimetre observations of ∊ Eridani and its surroundings*, Monthly Notices of the Royal Astronomical Society, Volume 462, Issue 3, p.2285-2294 (2016)

Event Horizon Telescope Collaboration, *First M87 Event Horizon Telescope Results. I. The Shadow of the Supermassive Black Hole*, The Astrophysical Journal Letters, Volume 875, Issue 1, article id. L1, 17 pp. (2019).

Gale, David M.; Hernández, Guillermo Becera; Rincón, Alejandra Ortega; Sosa, Martín. Tecuapetla; León-Huerta, Andrea; Cabrera Cuevas, Lizeth; Lucero Álvarez, Maribel; Tecuapetla Sosa, Esteban; Castro Santos, David; Tzile Torres, Carlos; Hernández Rios, Emilio, *Delivery of 20-micron surface segments for the 50-meter LMT primary reflector*, Proceedings of the SPIE, Volume 10706, id. 1070638 15pp. (2018a).

Gale, David M.; Schloerb, F. Peter; León Huerta, Andrea; Lucero Álvarez, Maribel; Cabrera Cuevas, Lizeth; Tecuapetla Sosa, Esteban; Castro Santos, David; Tzile Torres, Carlos; Hernández Rios, Emilio, *Photogrammetry mapping and alignment of the LMT 50-meter primary reflector*, Proceedings of the SPIE, Volume 10706, id. 1070646 15pp. (2018b).

Harrington, K. C.; Yun, Min S.; Cybulski, R.; Wilson, G. W.; Aretxaga, I.; Chavez, M.; De la Luz, V.; Erickson, N.; Ferrusca, D.; Gallup, A. D.; Hughes, D. H.; Montaña, A.; Narayanan, G.; Sánchez-Argüelles, D.; Schloerb, F. P.; Souccar, K.; Terlevich, E.; Terlevich, R.; Zeballos, M.; Zavala, J. A., *Early science with the Large Millimeter Telescope: observations of extremely luminous high-z sources identified by Planck*, Monthly Notices of the Royal Astronomical Society, Volume 458, Issue 4, p.4383-4399 (2016)

Heyer, M.; Wilson, G. W.; Gutermuth, R.; Lizano, S.; Gomez-Ruiz, A.; Kurtz, S.; Luna, A.; Serrano Bernal, E. O.; Schloerb, F. P., *Early science with the Large Millimetre Telescope: fragmentation of molecular clumps in the Galaxy*, Monthly Notices of the Royal Astronomical Society, Volume 473, Issue 2, p.2222-2233 (2018).

Mangum, J. G., Emerson, D. T, and Greisen, E. W. *The On-theFly Imaging Technique*, Astron. Astrophys. 474 679-687 (2007).

Ortiz-León, Gisela N.; Johnson, Michael D.; Doeleman, Sheperd S.; Blackburn, Lindy; Fish, Vincent L.; Loinard, Laurent; Reid, Mark J.; Castillo, Edgar; Chael, Andrew A.; Hernández-Gómez, Antonio; Hughes, David H.; León-Tavares, Jonathan; Lu, Ru-Sen; Montaña, Alfredo; Narayanan, Gopal; Rosenfeld, Katherine; Sánchez, David; Schloerb, F. Peter; Shen, Zhi-qiang; Shiokawa, Hotaka SooHoo, Jason; Vertatschitsch, Laura, *The Intrinsic Shape of Sagittarius A* at 3.5 mm Wavelength*,The Astrophysical Journal, Volume 824, Issue 1, article id. 40, 10 pp. (2016).

Schloerb, F. P.; Sanchez, D.; Narayanan, G.; Erickson, N.; Souccar, K.; Wilson, G.; Gale, D.; Hughes, David H.; Smith, D., *Calibration and operation of the active surface of the Large Millimeter Telescope*, Proceedings of the SPIE, Volume 9906, id. 99066C 7 pp. (2016).

Sun, Jiayi; Leroy, Adam K.; Schruba, Andreas; Rosolowsky, Erik; Hughes, Annie; Kruijssen, J. M. Diederik; Meidt, Sharon; Schinnerer, Eva; Blanc, Guillermo A.; Bigiel, Frank; Bolatto, Alberto D.; Chevance, Mélanie; Groves, Brent; Herrera, Cinthya N.; Hygate, Alexander P. S.; Pety, Jérôme; Querejeta, Miguel; Usero, Antonio; Utomo, Dyas, *Cloud-scale Molecular Gas Properties in 15 Nearby Galaxies*, The Astrophysical Journal, Volume 860, Issue 2, article id. 172, 39 pp. (2018).

Zavala, Jorge A.; Montaña, Alfredo; Hughes, David H.; Yun, Min S.; Ivison, R. J.; Valiante, Elisabetta; Wilner, David; Spilker, Justin; Aretxaga, Itziar; Eales, Stephen; Avila-Reese, Vladimir; Chávez, Miguel; Cooray, Asantha; Dannerbauer, Helmut; Dunlop, James S.; Dunne, Loretta; Gómez-Ruiz, Arturo I.; Michałowski, Michał J.; Narayanan, Gopal; Nayyeri, Hooshang Oteo, Ivan; Rosa González, Daniel; Sánchez-Argüelles, David; Schloerb, F. Peter; Serjeant, Stephen; Smith, Matthew W. L.; Terlevich, Elena; Vega, Olga; Villalba, Alan; van der Werf, Paul; Wilson, Grant W.; Zeballos, Milagros, *A dusty star-forming galaxy at z = 6 revealed by strong gravitational lensing*, Nature Astronomy, Volume 2, p. 56-62 (2018)